https://doi.org/10.1016/j.ymssp.2021.108383

An origami inspired QZS vibration isolator using a novel truss-spring based stack Miura-ori structure

Kan Ye*, J.C. Ji

School of Mechanical and Mechatronic Engineering, University of Technology Sydney

15 Broadway, Ultimo, NSW 2007, Australia

E-mails: kan.ye@uts.edu.au, jin.ji@uts.edu.au

Abstract

In this paper, an origami-inspired vibration isolator is proposed and numerically investigated to achieve a quasi-zero-stiffness (QZS) property. A truss-spring based stack Miura-ori (TS-SMO) unit structure is introduced in the vibration isolation system to provide a desired stiffness for high-static-low-dynamic requirement. Different from the traditional origami structures, which include rigid facets and deformable creases, the proposed TS-SMO structure uses coil springs to replace all creases, so the physical realization can be implemented into engineering applications. Nonlinear force response and unique features can be achieved through its geometric nonlinearity and Poisson's ratio profile. The static features and working principles of the developed TS-SMO structure are numerically discussed to meet specific feature requirements first. Then a QZS vibration isolator is presented under specific parameter design. The force-displacement response and stiffness diagram are obtained to verify the static performance of the isolation system. Furthermore, the displacement transmissibility is derived through dynamic analysis by employing the harmonic balance method (HBM). The isolation performances under variable viscous damping are also discussed to show the effects of system damping.

Keywords

Vibration isolation, Quasi-zero-stiffness, Nonlinear vibration isolator, Origami structure, Transmissibility

1. Introduction

Quasi-zero-stiffness (QZS) system have recently received much attentions from researchers and engineers as nonlinear vibration isolator. For a traditional linear spring-mass isolator, the isolation performance can only be achieved beyond $\sqrt{2}$ times of its natural frequency. In order to prevent the damages from low-frequency harmful excitations, soft spring with lower stiffness can be selected to obtain a low natural frequency but this would lead to another issue in real applications: large static deflection. Thus, the high-static-low-dynamic stiffness (HSLDs) characteristic was developed to overcome this drawback. A small static deflection and low natural frequency for a targeted loading can be realized through the design of the QZS system.

A typical QZS system includes a high positive stiffness structure and a corresponding negative stiffness system. A high value of the positive stiffness element can ensure a reasonable static deflection; while the negative stiffness system with a narrower workable range could reduce the total stiffness around the targeted loading capacity, thus the dynamic stiffness can be reduced and the isolation performance can be improved. Different stiffness structures can be used individually or in various combinations. Coil springs which can provide linear stiffness are widely used in different mechanisms due to their easily physical realization [1, 2], to formulate the negative stiffness element. Zhao et. al. [3] theoretically and experimentally investigated the QZS isolator using two pairs of oblique springs and improved the system performance [4]. Other nonlinear stiffness structures have been used in the QZS design, such as magnetic springs [5-8], which can provide the nonlinear stiffness directly. Zheng et. al. [6] developed a magnetic vibration isolator which combined magnetic rings and a spiral flexure spring. The isolation performance was verified through both simulations and experiments that can extend the isolation frequency band. Pu et. al. [9] proposed a semi-active isolation system with tunable negative stiffness. Multi-layer electromagnetic springs were used to generate the negative stiffness and perform a tunable HSLDs characteristic. Both theoretical and experimental results verified the isolation performance within certain frequency band. Jiang et. al. [10] developed a QZS isolator using the electromagnetic and air spring technology. The other method to generate a nonlinear QZS system can be using structures with geometric nonlinearity. Zou et. al. [11] analysed the QZS system performance with a scissor-like structure. Isolation of high-amplitude excitation in resonant region were reported beside the

normally discussed low frequency vibration isolation. Bio-inspired structures have also been used to create the nonlinear stiffness due to their geometric nonlinearity [12-15]. Jiang et. al. [13] presented a novel bio-inspired anti-vibration structure to demonstrate the high-static-low-dynamic stiffness characteristic and subject to large vibration amplitude. Unique nonlinear property and large compression displacement range were carried out by using a multi-joint limb-like structure.

As discussed in a recent literature review paper [16], the origami-based structure, known as a nonlinear morphing system , can be introduced in the design of QZS system for vibration isolation. The origami-based structure has some specific features, including compact deployment, bistable states, self-deployable ability, and nonlinear force-displacement relationships. Either the bistable ability or the unique geometry characteristic can be adopted to generate the HSLD characteristic. Origami base structures can be formed from different patterns of the origami unit structures which have potential applications in vibration isolation[16]. The stack Miura-ori (SMO) pattern, a double-layer structure which is typically stacked by two Miura-ori patterns, shows different geometric folding patterns and variable Poisson's ratio [17]. For traditional crease-based origami structure, the facets are normally surrounded by creases, and the torsional spring stiffness for each crease is assigned corresponding to their individual lengths and folding conditions. Two different lengths and five groups of folding angles can be defined to determine the kinematic relationships. However, an easily physical realization of the origami structures using simple mechanical structures is still a challenge in implementing engineering applications, and this may be one of the main reasons to limit the wide application of origami structures in practical engineering. Either the vertex which joint multiple creases or the creases themselves would be deformed with related motions to others during the morphing process. This means the link/connection between the origami structure and the support structure could either affect the crease performance or result in a local coordinate change related to the system (global) coordinate; and hence the overall performance of the origami-based structures would be changed. In addition, the initial stress-free condition of the origami structure is important and sensitive, which requires a careful design and accurate manufacturing. In the reported experiments, the rigid facets are normally fabricated separately and then joined through hinges or plastic film [18]. The creases which provide the torsional stiffness can be replaced by using pre-bent spring steel strip or torsional springs. Other methods, such as 3D AM print method were also used to experimentally confirm the origami designs [19]. Although few lab-controlled experiments were conducted [20-23], the real

applications were rare to find. According to the literature review and the authors' knowledge, the current material selection and fabrication method cannot fully meet the requirements of the origami structure, which has limited its applications.

Therefore, in this paper, a novel truss-spring SMO base structure is proposed first to replace the traditional crease-based origami structure. Linear coil springs are applied to replace the creases and provide linear stiffness along the directions of creases. By transforming through its compatible geometry and complex structure linkage, nonlinear system stiffness can be obtained in certain directions. Hence, the physical realization of origami-based structures can be implemented while similar features to the crease-based origami structure can be maintained. With a careful design and geometric parameter analysis, a high-static-low-dynamic QZS vibration isolator will be presented. The force-displacement response and stiffness characteristics will be investigated to verify its static performance. Then the displacement transmissibility is derived through dynamic analysis by employing the harmonic balance method (HBM). The effect of the isolation performance due to the system damping is also discussed as it was found the damping has a significant effect on the resonance response [24].

The rest of this paper is organized into three sections: Section 2 presents the new truss-spring SMO base structure. The effects of the design parameters on the system performance are discussed individually first and then in various combinations to perform the unique features; Section 3 numerically studies the static performance and dynamic behaviour of the proposed QZS system using the TS-SMO structure. The concluding remarks are summarized in Section 4.

2. Modelling of the Truss-Spring SMO

To avoid the fabrication difficulties of the crease-based origami structure, a novel truss-spring structure is proposed to replace all creases in a SMO base structure, as shown in Figure 1. Different from the tradtional crease-based SMO, free-torsion hinges are used at the crease locations and three sets of coil springs are applied in each principal direction. All springs are of positive stiffness, while pre-stressed conditions could determine the spring types as compression or tension springs, but which would also be limited by the type. The nonlinear variable Poisson's ratios of the unit structure in the principal directions could lead to different deformation conditions to the springs, and the resulting forces can be transformed through the

compatible geometry and complex motional compatibility. Thus, similar force responses and unique features to the original crease-based origami structure can be achieved but with easy realization in practical applications.

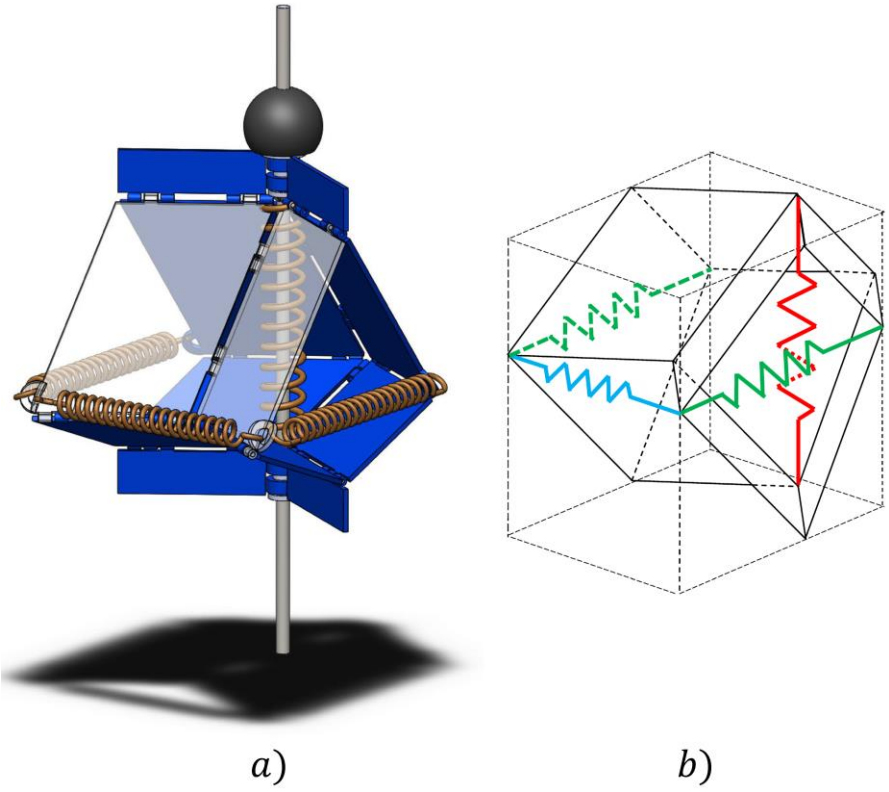

Figure 1 Schematic of the proposed TS-SMO base structures: (a) 3D model and (b) simple schematic of the spring setup

2.1. Geometric configurations of the SMO unit cell

The typical SMO unit structure is composed of two layers of standard Miura-ori sheet, as shown in Figure 2(a) and (b). Certain parameter relationships between each sheet should be followed to ensure the facet rigidity and motional compatibility. Specifically, the sides of each facet at the connecting surface from both sheets share the same parameters ($b_I = b_{II} = b$). The sector angles to the other side (γ_I, γ_{II}) and the other side's lengths (a_I, a_{II}) can be independent but need to satisfy the relations:

$$\frac{\cos\gamma_{II}}{\cos\gamma_I} = \frac{a_I}{a_{II}} \quad (1)$$

$$\frac{\cos\theta_{II}}{\cos\theta_I} = \frac{\tan\gamma_I}{\tan\gamma_{II}} \quad (2)$$

where θ_I and θ_{II} are the dihedral folding angles of the facets on each sheet to the reference panel (*ref panel* as shown in Figure 2 (b)). According to the folding condition and the related states of the two Miura-ori unit structures, two states can be named as convex state and concave state, respectively as shown in Figure 2 (c). For clarity, when Sheet I is nested-in and its dihedral folding angle $\theta_I > 0°$, the stable state is referred to "concave" state; otherwise, it is defined as "convex" state. Without considering the thickness of the facet and possible physical collision at the crease location, the dihedral folding angles of the facet on Sheet I to the reference panel (θ_I) is variable in the range of [-90° 90°], which can also be used to indicate the folding condition of the SMO unit theoretically from 0% to 100%. When the bottom Sheet I is fully nested-in ($\theta_I = 90°$), the SMO unit is at 100% folding; and when the Sheet I is fully bulged-out ($\theta_I = -90°$), the SMO unit is at 0% folding.

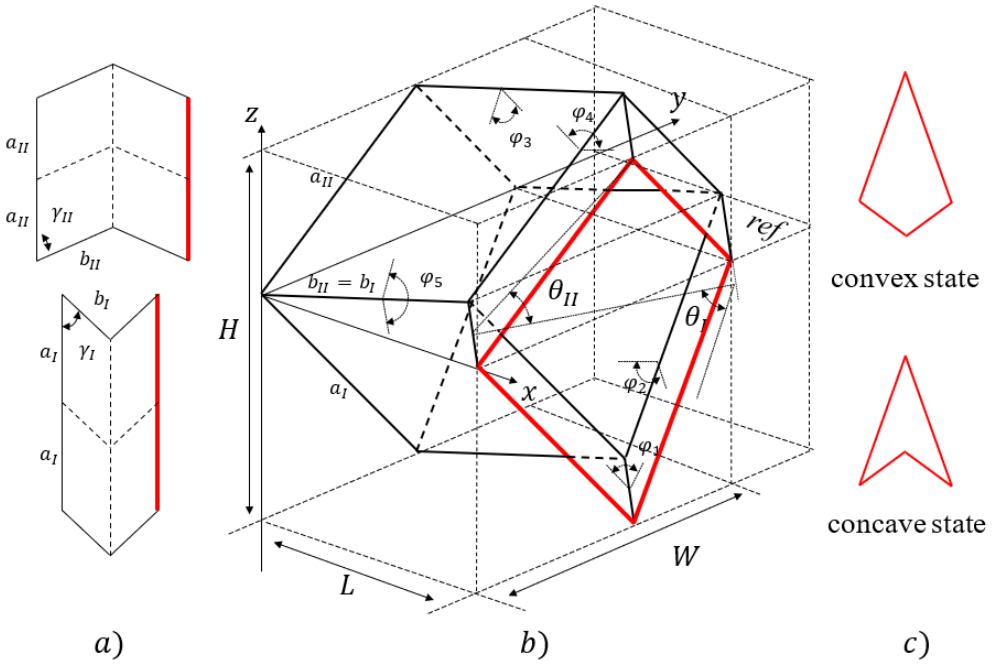

Figure 2 Typical SMO structure: (a) Miura-ori sheets with different parameters; (b) 3D SMO unit cell and (c) its bi-stable states

The external dimensions of the SMO cell can also be expressed by using the dihedral folding angles (θ_I):

$$\begin{cases} L = \frac{2b_I \cos\theta_I \tan\gamma_I}{1+\cos^2\theta_I \tan^2\gamma_I} \\ W = 2a_I\sqrt{1-\sin^2\theta_I \sin^2\gamma_I} \\ H = a_I \sin\gamma_I \left(\sqrt{\frac{\tan^2\gamma_{II}}{\tan^2\gamma_I} - \cos^2\theta_I} - \sin\theta_I\right) \end{cases} \quad (3)$$

where L, W and H represent the length, width and height of the SMO unit in the x-y-z coordinate as shown in Figure 2(b).

The Poisson's ratios of the unit structure can be defined as [17, 25]

$$\begin{cases} \nu_{HL} = -\dfrac{\Delta L/L}{\Delta H/H} \\ \nu_{HW} = -\dfrac{\Delta W/W}{\Delta H/H} \end{cases} \tag{4}$$

Both Poisson's ratios (ν_{HL}, ν_{HW}) with respect to different sector angles of the facet in Sheet I (γ_I) are illustrated in Figure 3 (a) and (b). It is easy to notice that when folding from convex state to concave state, the Poisson's ratio in both horizontal directions with respect to the vertical direction are dropping from a positive to negative value. The turning boundaries are both located at 50% folding condition, when the folding angle is $\theta_I = 0°$ and Sheet I is flatten. There are differences between the different horizontal directions ν_{HL} and ν_{HW} with different facet shapes. When the sector angle (γ_I) is increasing from 40° to 80°, the changes of the Poisson's ratios in two horizontal directions are opposite; ν_{HL} is decreasing while ν_{HL} is increasing. This means, when using a low sector angle (γ_I) facet, the deformation of the unit structure in the L direction with respect to the deformation in the H direction is lower than using a high sector angle facet; meanwhile the deformation in the W direction is higher. It is also observed that the facet length (a_{II}) can also affect the Poisson's ratios (ν_{HL}, ν_{HW}). Both Poisson's ratios could be increased when a longer facet length (a_{II}) is used. However, it has insignificant influence when compared to the effect due to the sector angle (γ_I).

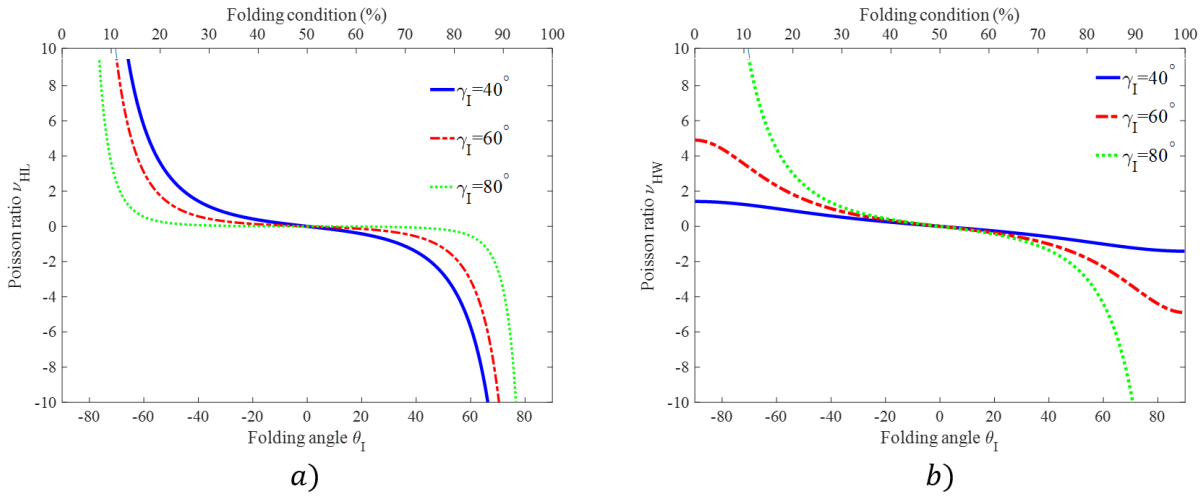

Figure 3 Poisson's ratios with respect to different sector angle (γ_I) of Sheet I facet: a) ν_{HL} and b) ν_{HW}

Since rigid origami structure is considered and the bending energy of all facets is assumed to be 0, the total potential energy of the SMO unit structure can then be calculated as a summation of the elastic potential energy of each spring. Thus,

$$U_{\text{total}} = \sum U_{\text{spring}} = \frac{1}{2}\sum_{i=1}^{n} K_i(l_i - {l_i}^0 + {\delta_i}^0)^2 \qquad (5)$$

where n is the total number of the springs within the SMO unit structure and K_i is the corresponding spring stiffness. l_i is the effective length of spring at a specific folding condition, which is equal to the external dimensions of the unit structure in this study, ${l_i}^0$ and ${\delta_i}^0$ are the initial length and pre-compression/extension of spring at the reference state of the SMO unit, which can be specified by using the initial folding condition θ_I^0 $(or\ \theta_0)$.

By differentiating the total potential energy with respect to the deformation in its principal directions (i.e., the L-W-H direction in terms of x-y-z coordinate as shown in Figure 2(b)), the force-deformation relationships and stiffness responses can be obtained as:

$$\begin{cases} F_X = \frac{dU_{crease}}{dX} = \frac{dU_{crease}}{d\theta}\left(\frac{dX}{d\theta}\right)^{-1} \\ K_X = \frac{dForce_X}{dX} = \frac{dU_{crease}}{d\theta}\left(\frac{dX}{d\theta}\right)^{-2} \end{cases} for\ X = L, H, W \quad (6)$$

Figure 4 illustrates the anisotropy force-deformation relationships of the SMO unit based on a particular design parameter set: $a_I = b, a_{II} = 1.5b, \gamma_I = 60°,\ k_L = k_H$ and $k_W = k_H$. The simulation of the SMO folding process is started from a reference state at convex state with $\theta_I^0 = -60°$. Due to the strongly nonlinear Poisson's ratios, the force responses have shown significant differences between principal axes, especially the vertical *H* direction to the horizontal *L* and *W* directions. The relatively high responses close to the maximum deformation in each direction are unstable states due to the rigid facet and the motional compatibility. Thus, only the deformation range between $[-60°\ 60°]$ is considered and discussed. It can be clearly noted that the responses appear mono-stable in the horizontal *L* and *W* directions. Both equivalent system stiffness in the horizontal directions are nonlinear but only with insignificant differences during two unidirectional folding processes (switch between convex and concave states). However, in the *H* direction, an obvious snap-through behaviour occurs. The equivalent system stiffness in the vertical direction becomes significantly different when switching between its two stable states. According to the variable nonlinear Poisson's ratios and the coil springs applied in the TS-SMO structure, the anisotropic distributions of the unit structure can enable desired structure properties through the spring type and stiffness selections.

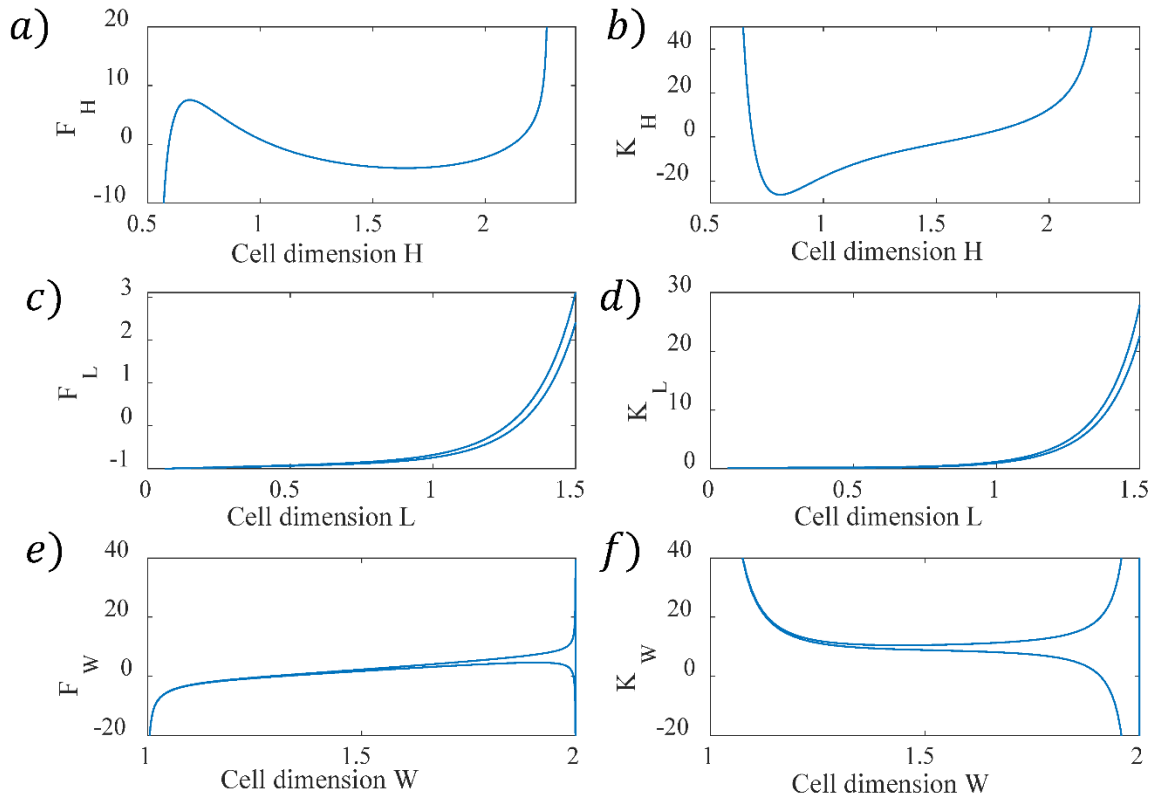

Figure 4 Anisotropy force-deformation relationships of the SMO unit cell

2.2. Effects of spring parameters on the static performance

It should be noted that both variable Poisson's ratios and spring properties can affect the overall performance of the SMO unit structure. The Poisson's ratios are determined only by the geometric parameters of the facets. With different designs, only the magnitudes of Poisson's ratios change while the variation tendency (curve shape) remains same, as discussed previously. Thus, even though the geometrically-parametric design is essential, comprehensive consideration of the Poisson's ratios and other factors is predictable and a further discussion is unnecessary. Thus, only the spring parameters that could significantly change the overall performance will be discussed in this section. Since the deformation in the *H* direction exhibits more bi-stable feature than the other two directions according to their Poisson's ratios, the subsequent analysis and discussion will be focused on the responses in *H* direction during folding and it is assumed that a convex state when $\theta_I^0 = -60°$ is the reference state.

As previously stated, two types of coil springs can be applied in the form of compression spring or tension spring. Due to the physical consideration, tension spring should not be compressed

and compression spring cannot provide stiffness during extension. This means that there exist limits for pre-stressed conditions in the analysis according to the spring type: tension spring should not have pre-compression; and the pre-compressed condition should be remained for releasing compression spring. In this particular comparative analysis, the equivalent stiffness in both horizontal directions use a unit stiffness value k_H, and the pre-compression/extension length use a unit length b (unit length of the shared facet side).

By applying the spring sets in *L* or *W* direction separately and individually, the force responses and stiffness responses with respect to the compression of the unit structure in the *H* direction are shown in Figure 5 and Figure 6.

Figure 5 (a) and (b) shows the force responses and stiffness responses with respect to the compression of the unit structure in the *H* direction when different springs are applied in the *L* direction only. Tension spring is assumed to be used with a positive pre-extension length when at the reference convex state. On the contrary, compression spring is assumed to be used with a negative pre-compression length. According to the Poisson's ratios, low stiffness is provided around the 50% folding, and high stiffness is provided when the folding is closer to the maximum or minimum folding. It is also interesting to find that the stiffness response in the *H* direction provided by a compression spring in *L* direction with a pre-compression length at reference state is also positive; while using a tension spring with pre-extension, the sign of the stiffness is switched from negative to positive with a "valley" response when closer to the minimum folding (a large value of the dimension *H*). Figure 6 (a) and (b) similarly displays the force and stiffness responses but with different springs applied in the *W* direction. Almost identical stiffness response is clarified when using compression spring in *W* direction to *L* direction. However, while a tension spring is used, a difference appears when close to the maximum and minimum folding condition: the negative stiffness response when towards the maximum folding is reduced and tends to become positive with a "valley" response. On the other hand, when towards the minimum folding, the stiffness response is increased and changes its sign smoothly without a "valley" response.

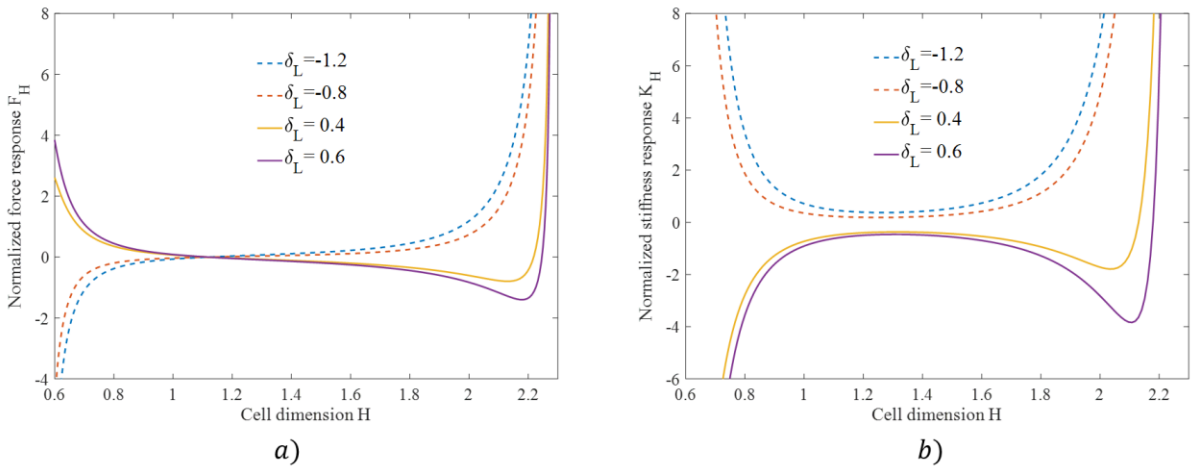

Figure 5 Normalized force and stiffness response in the H direction when different springs applied in the L direction only

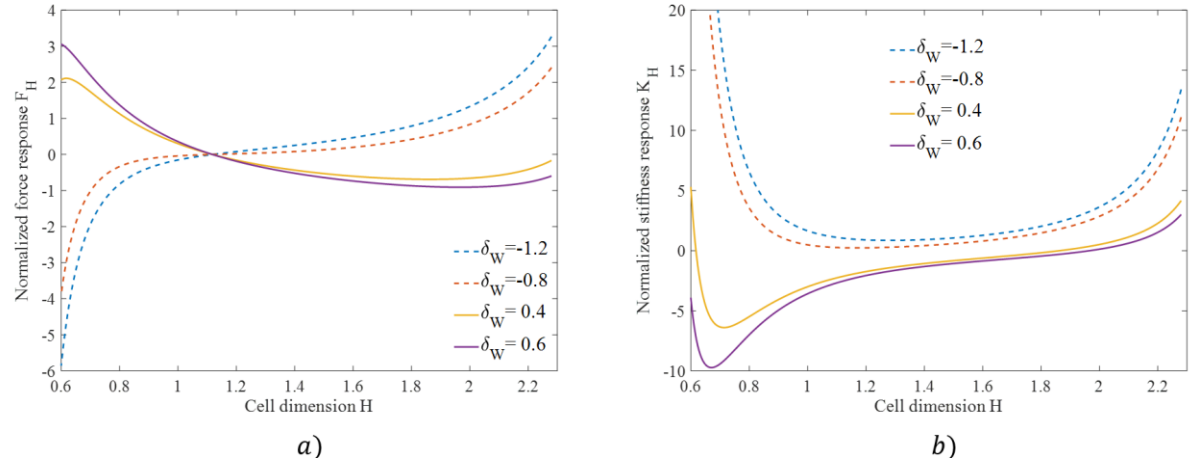

Figure 6 Normalized force and stiffness response in the H direction when different springs applied in the W direction only

Since the relationship between the deformation in the vertical *H* direction and the force response due to a vertical spring in the same direction is linear, the spring type in the *H* direction is not important under restrictions and its stiffness response would always be a positive constant. Thus, when assembling all three sets of springs in each principal direction, different features of the proposed TS-SMO structure can be achieved. The snap-through behaviour can be generated when the positive stiffness is reduced to negative in a unidirectional folding, either from maximum to minimum folding or vice visa. Thus using at least one tension spring set in the horizontal direction could provide high negative stiffness component to reduce the total stiffness in the vertical direction. Moreover, minimizing the snap-through behaviour could result in the QZS characteristic. Two particular designs are presented in Figure 7.

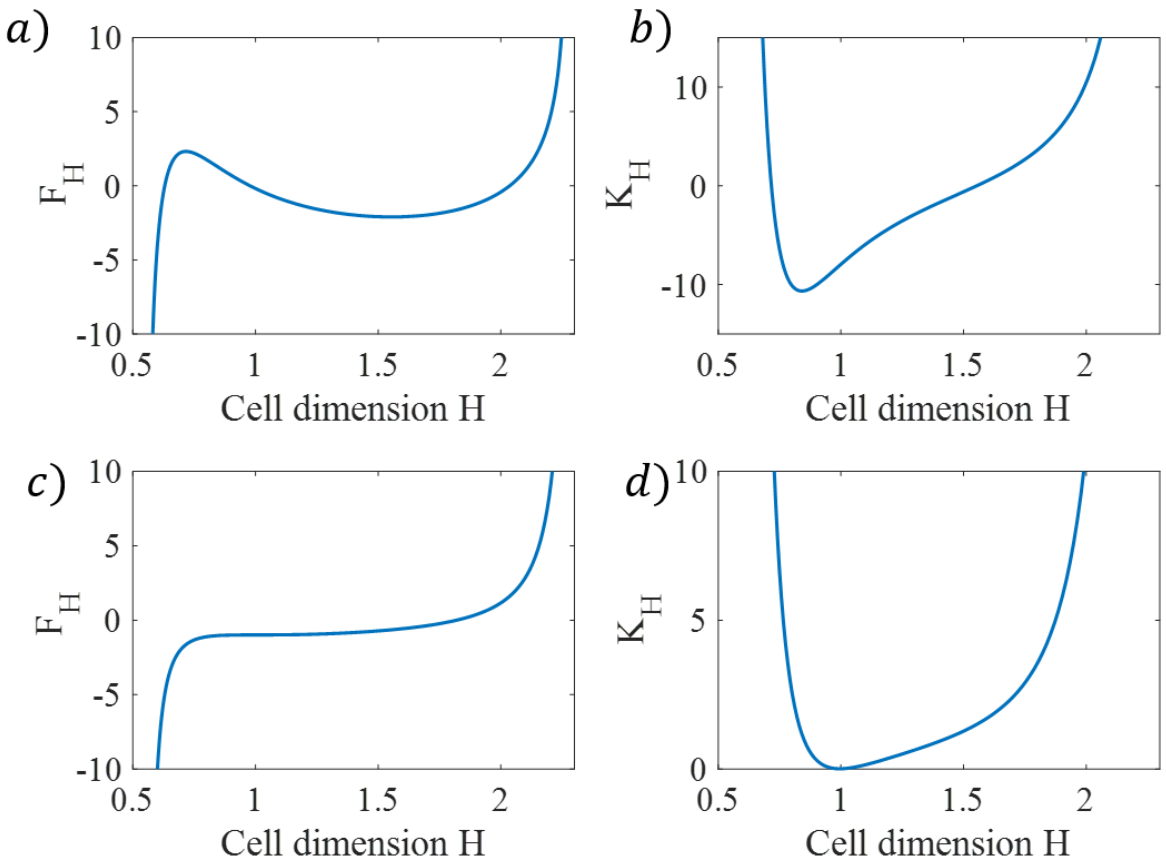

Figure 7 Force and stiffness responses of two examples that state the unique features can be achieved: (a-b) Bistable with snap-through behaviour, particular design parameters as:($k_L k_W k_H$)= *(0.5 5 1) and* (δ_L δ_W δ_H)= *(0 -1 0) and (c-d) QZS, particular design parameters as:*($k_L k_W k_H$) = (1.2 1 1) *and* (δ_L δ_W δ_H) = *(0 -1.2 0)*

3. QZS application using the TS-SMO structure

This section presents a QZS vibration isolator as an application example of the TS-SMO structure. The proposed QZS system included a TS-SMO unit structure and a loading platform placed at the top of the unit structure. The schematic diagram of the proposed structure is shown in Figure 8. The initial state of the TS-SMO base structure is designed at a convex state and the loading platform is placed at the reference position H^0. When a weight is applied on the loading platform, the static equilibrium position is changed to H^S by compressing the unit structure with a distance d_m. It is assumed that a convex state when $\theta_I^0 = -60°$ is the reference state, and the compression of the base structure in each direction at the reference state are (L,W,H)=(0 0 0). The parameters should be carefully designed to avoid the possible snap-through behaviour.

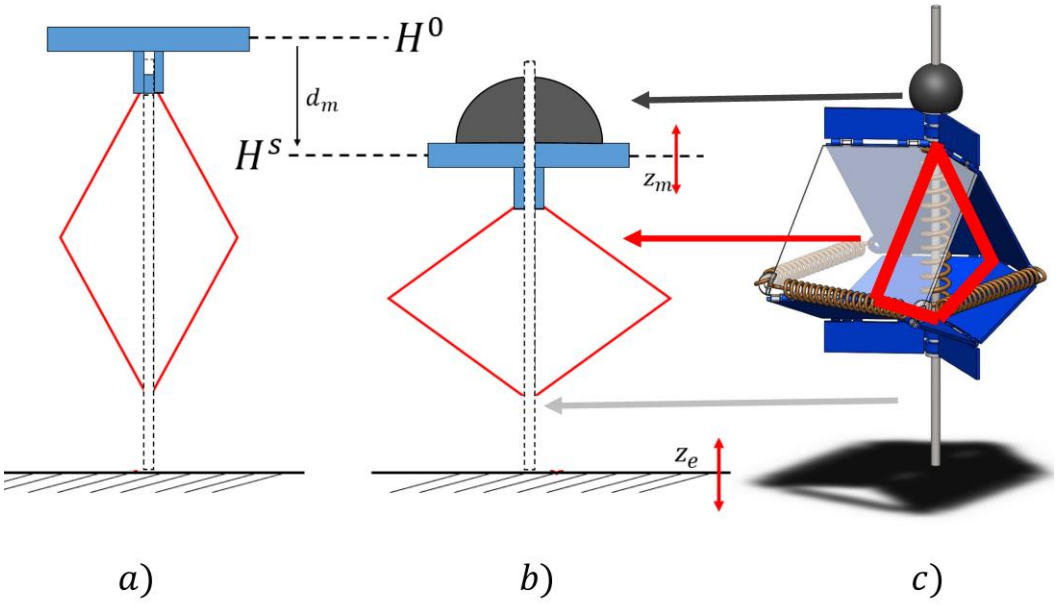

Figure 8 Schematic diagram of the proposed TS SMO QZS system: (a) initial reference state, (b) loading applied state and (c) 3D structure diagram

The optimization of the parameter design requires that the stiffness in the working zone is always positive and the minimum stiffness is close to 0 for a better isolation performance, which is

$$mg = f(H^S) = F_{(H^0 - d_m)}, \text{ where } K_{(H^S)} \geq 0 \ \& \ K_{min} \to 0^+ \qquad (7)$$

Table 1 lists the design parameters of the TS-SMO unit with this particular design. According to Eq.(3) and Eq.(4), the nonlinear compressions in the principal directions can be calculated and are shown in Figure 9.

Table 1 design parameters of the TS-SMO unit structure for the QZS system

SMO structure parameters (at the initial reference state)			
a_I	1b	θ^0	-60°
a_{II}	1.5b	γ_I	60°
Coil spring parameters (at the initial reference state)			
	Stiffness k_X	Pre-stress δ_X	Spring type
H	k_H	0	Compression
W	k_H	0	Tension
L	$1.2k_H$	-1.2b	Compression

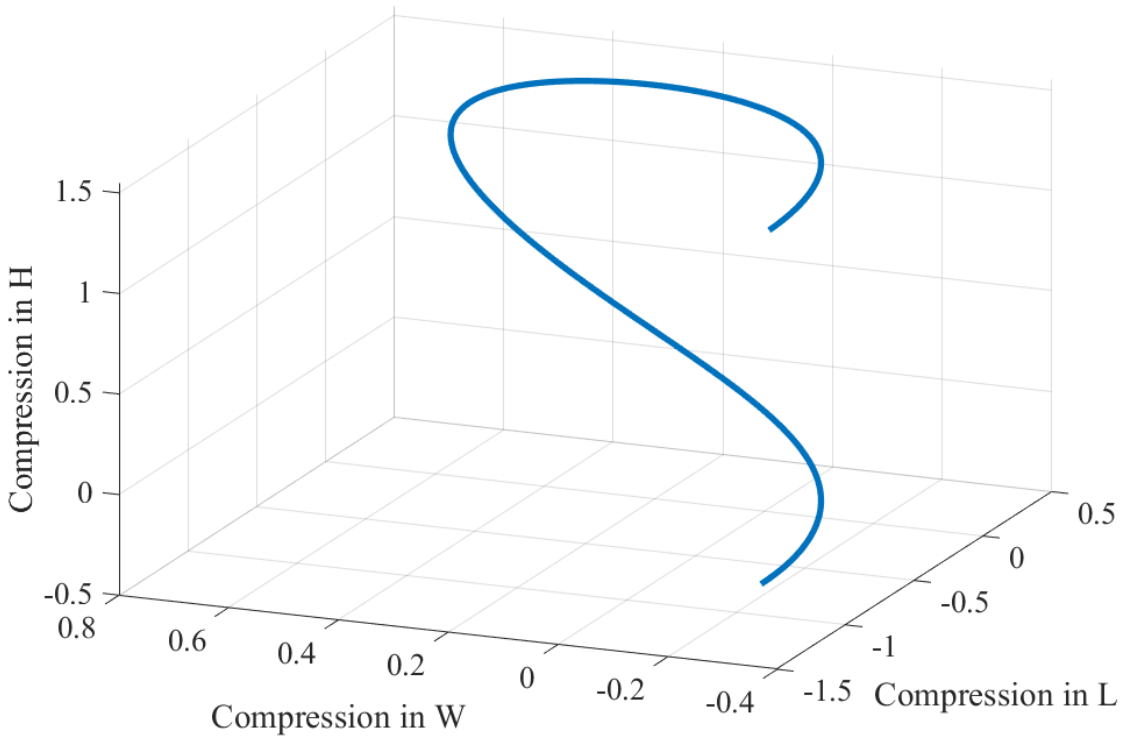

Figure 9 Relationships of the compression/extension state in each principal directions: Positive value states a compression deformation of the unit cell to the referent state and negative value states an extension deformation

The force response and equivalent system stiffness in the vertical direction versus the vertical compression can be obtained from Eq.(6), as shown in Figure 10. The stiffness response is asymmetric about the minimum stiffness position. And the minimum stiffness occurs when the compression is $d_m = 1.1056$.

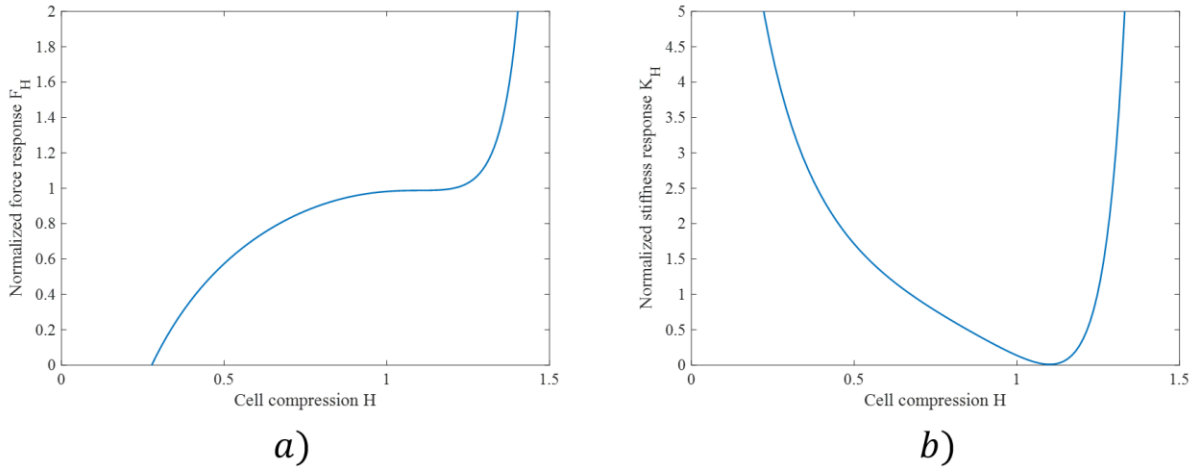

Figure 10 (a) force response and (b) stiffness response of the proposed TS SMO QZS system

By using the least squares (LS) method, a third-order polynomial best fitting line of the force response of the TS-SMO structure can be obtained as

$$F_{(x)} = \alpha_3 x^3 + \alpha_2 x^2 + \alpha_1 x + \alpha_0 \qquad (8)$$

When different compression ranges are applied around the minimum stiffness position, different polynomial constants can be obtained and are listed in Table 2. The error analysis between the fitted force response curves and the analytical results can be performed using the equation $E = \frac{F_{bestfit} - F_{analytic}}{F_{analytic}} \times 100\%$, as illustrated in Figure 11, where E denotes the error. It is worth noting that although the best fitting line from a narrow compression range around the minimum stiffness position can largely preserve the response properties, the error increases quickly outside the narrow range; while the best fitting line with a middle compression range has an acceptable error range (within 0.5%) but with a wider compression range. Hence, the polynomial constants from a middle compression range about the minimum stiffness position will be selected for further equivalent dynamic analysis.

Table 2 the three-order polynomial constants of best fitting approach using LS method in different compression range

Polynomial constants	Compression range		
	Wide ($d_m \pm 0.2b$)	Middle ($d_m \pm 0.1b$)	Narrow ($d_m \pm 0.05b$)
α_3	7.5474	5.6415	6.9827
α_2	-23.698	-18.201	-22.959
α_1	24.771	19.590	25.172
α_0	-7.638	-6.048	-8.2161

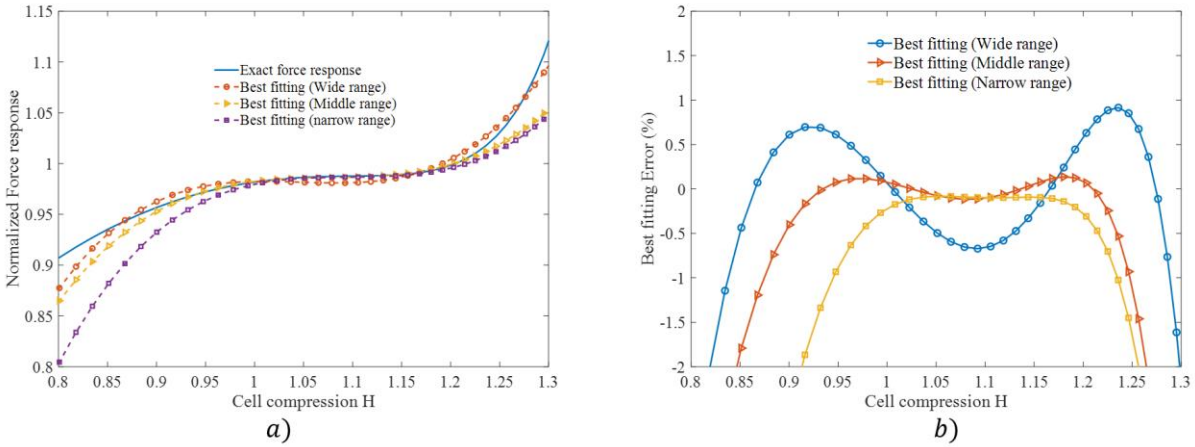

Figure 11 (a)Exact force response and its approximation using LS method and (b) the errors when different compression ranges used.

3.1.Dynamic analysis and parameter discussion

When an absolute excitation z_e is applied to the base of the isolation system, the relative position u of the loading platform with reference to the base of the system can be defined as

$$u = d_m + y \qquad (9)$$

where $y = z_m - z_e$ is the relative motion to the static equilibrium position and z_m is the absolute position of the loading platform.

Thus, the equation of the motion of the loading platform under the harmonic displacement excitation z_e can be written as

$$m\ddot{u} + c\dot{u} + f_{(u)} = mg - m\ddot{z}_e \qquad (10)$$

It can then be simplified by substituting Eq.(8) and Eq.(9) as

$$\ddot{y} + \frac{c}{m}\dot{y} + \frac{\alpha_3}{m}y^3 + \frac{3\alpha_3 d_m + \alpha_2}{m}y^2 + \frac{2\alpha_2 d_m + 3\alpha_3 {d_m}^2 + \alpha_1}{m}y = -\ddot{z}_e \qquad (11)$$

By assuming the harmonic displacement excitation $z_e = Z_e \cos(\omega t + \varphi)$, letting the non-dimensional parameters $\bar{y} = \frac{y}{Z_e}, \Omega = \frac{\omega}{\omega_n}, \tau = \omega_n t, \hat{y}' = \frac{\dot{\bar{y}}}{\omega_n}, \hat{y}'' = \frac{\ddot{\bar{y}}}{{\omega_n}^2}, \xi = \frac{C}{2m\omega_n}, \beta_3 = \frac{\alpha_3}{\alpha_1}{Z_e}^2, \beta_2 = \frac{3\alpha_3 d_m + \alpha_2}{\alpha_1}Z_e, \beta_1 = \frac{2\alpha_2 d_m + 3\alpha_3 {d_m}^2 + \alpha_1}{\alpha_1}$, and making $\omega_n = \sqrt{\alpha_1/M}$ as the undamped

natural frequency for the corresponding linear system, the equation of motion of the proposed TS-SMO QZS system can be obtained as

$$\hat{y}'' + 2\xi\hat{y}' + \beta_3\hat{y}^3 + \beta_2\hat{y}^2 + \beta_1\hat{y} = \Omega^2\cos(\Omega\tau + \varphi) \qquad (12)$$

Further by assuming the general solution $y = Y\cos(\Omega\tau)$ and applying the harmonic balance method (HBM), the equation of motion can be expressed as:

$$\left(-\Omega^2\hat{Y} + \frac{3}{4}\beta_3\hat{Y}^3 + \beta_1\hat{Y}\right)\cos(\Omega\tau) + \left(-2\xi\Omega\hat{Y}\right)\sin(\Omega\tau) + \beta_2\hat{Y}^2\left(\frac{1+\cos(2\Omega\tau)}{2}\right) +$$
$$\beta_3\hat{Y}^3\left(\frac{\cos(3\Omega\tau)}{4}\right) = \Omega^2\cos(\varphi)\cos(\Omega\tau) - \Omega^2\sin(\varphi)\sin(\Omega\tau) \qquad (13)$$

Neglecting the high-order terms and equating the coefficients for $\cos(\Omega\tau)$ and $\sin(\Omega\tau)$ yields

$$\begin{cases} \beta_1\hat{Y} - \Omega^2\hat{Y} + \frac{3}{4}\beta_3\hat{Y}^3 = \Omega^2\cos(\varphi) \\ 2\xi\Omega\hat{Y} = \Omega^2\sin(\varphi) \end{cases} \qquad (14)$$

Squaring the both sides of Eq. (14) and adding the resultant equations, leads to the amplitude-frequency equation:

$$\frac{9}{16}{\beta_3}^2\hat{Y}^6 + \frac{3}{2}(\beta_1 - \Omega^2)\beta_3\hat{Y}^4 + ((\beta_1 - \Omega^2)^2 + 4\xi^2\Omega^2)\hat{Y}^2 - \Omega^4 = 0 \qquad (15)$$

This amplitude-frequency response equation can be solved in Matlab to obtain a relationship between the relative vibration transmissibility $\hat{Y} = \frac{Y}{Z_e}$ and the non-dimensional excitation frequency $\Omega = \frac{\omega}{\omega_n}$. The absolute vibration transmissibility can be calculated from the ratio of the absolute displacements of the weight and the base by:

$$Ta = \left|\frac{Z_m}{Z_e}\right| = \frac{\sqrt{Y^2 + Z_e^2 + 2YZ_e\cos\varphi}}{Z_e} \qquad (16)$$

By introducing the non-dimensional form $\hat{Y} = Y/Z_e$ and Eq. (14), the absolute displacement transmissibility of the proposed QZS system can be expressed as:

$$Ta = \sqrt{1 + \left(\frac{2\beta_1}{\Omega^2} - 1\right)\hat{Y}^2 + \frac{3\beta_3}{2\Omega^2}\hat{Y}^4} \quad (17)$$

For comparison purpose, the vibration transmissibility of the corresponding linear system with the undamped natural frequency ω_n is given by:

$$\begin{cases} \hat{Y} = \sqrt{\frac{\Omega^4}{1-2\Omega^2+4\xi^2\Omega^2+\Omega^4}} \\ Ta = \sqrt{\hat{Y}^2 + 1 + \frac{2(1-\Omega^2)}{\Omega^2}\hat{Y}^2} \end{cases} \quad (18)$$

As clearly shown the displacement transmissibility under different excitations in Figure 12, the QZS isolation performance can be achieved in low frequency range by using the TS-SMO structure. Similar to any other QZS isolators, transmissibility and its resonance frequency are sensitive to excitation magnitude and the damping coefficient. When a larger excitation is applied to the weight, the jump phenomenon would occur in the response. In order to investigate the effect of system damping on the resonance frequency, the displacement transmissibility under various damping ratios are compared and shown in Figure 13. The system damping ratio is increased from 0.020 to 0.023 until the unstable region is vanished. It can be observed that the system damping ratio can significantly reduce the resonance amplitude and lower the peak frequency. However, it would slightly increase the transmissibility in the off-resonance region and reduce the isolation performance. Hence, a certain amount of viscous system damping should be considered in real practical applications for damping the transient state to stable state and reducing the resonance response.

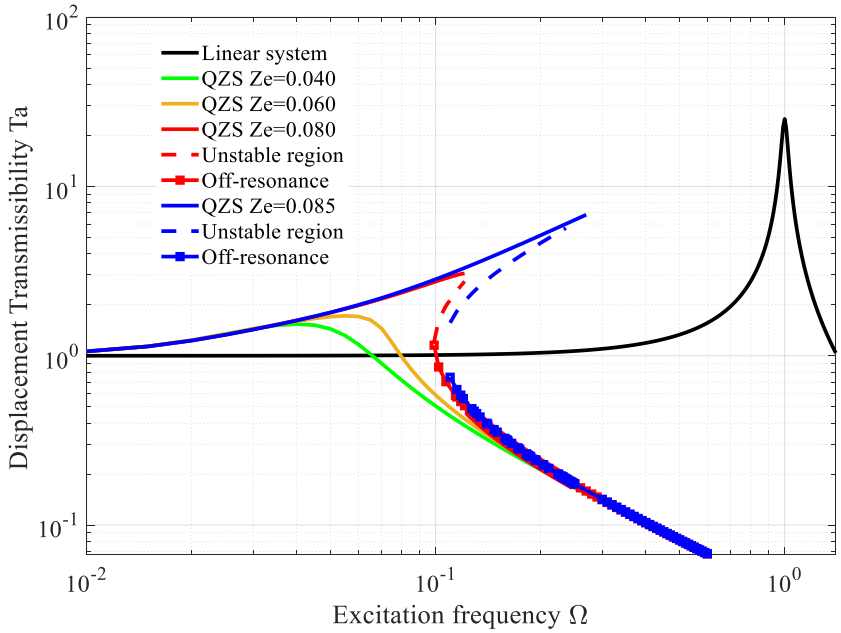

Figure 12 Absolute displacement transmissibility of the proposed TS-SMO QZS system under different excitations when system damping $\zeta = 0.02$ is applied

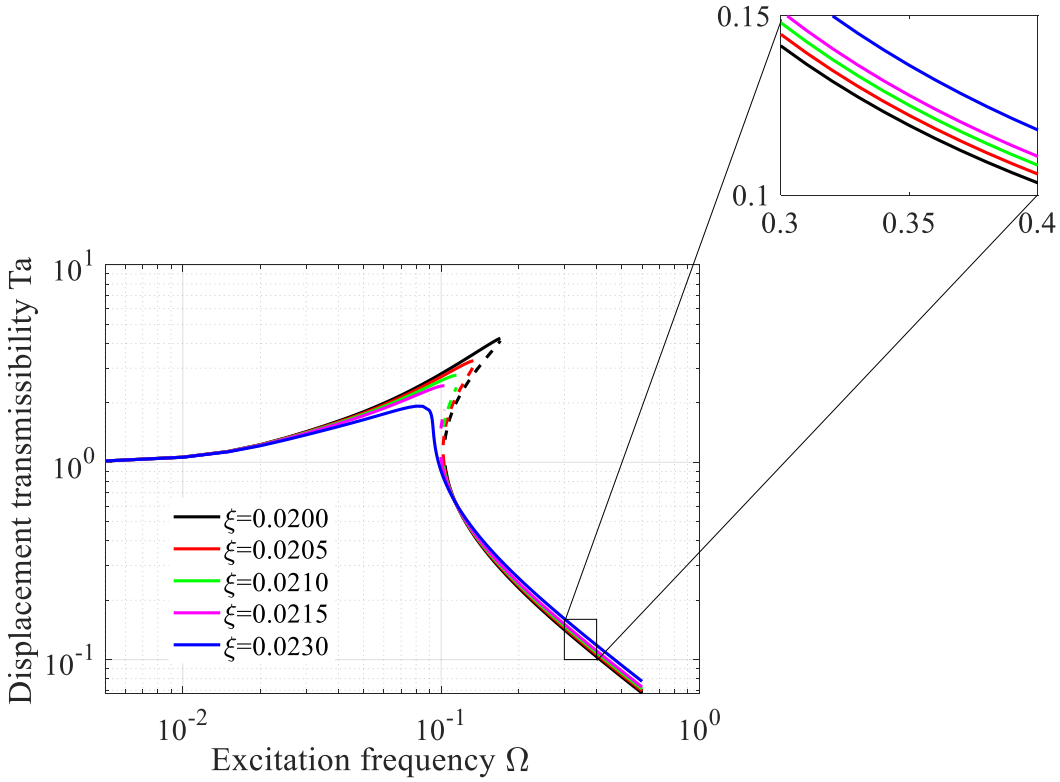

Figure 13 Absolute displacement transmissibility when different system damping ratios ($\zeta = 0.020 - 0.023$) are applied and $Z_e = 0.083b$

4. Conclusion

This paper proposed a novel truss-spring SMO unit structure and its application to QZS system. In order to implement the physical realization of using origami structure in engineering applications, a truss-spring SMO structure has been developed and discussed first by using normal coil springs to replace the deformable creases in the origami-based structure. The unique variable Poisson's ratios of the unit structure could generate nonlinear deformation response in the principal axis direction and the force response from the springs applied in the principal axis direction can be transformed through the compatible geometry to provide a desired system performance. The geometric parameter designs of the facets to the Poisson's ratios of the SMO unit, the spring selection and configuration have been discussed separately to study the overall performance. With an appropriate design of system parameters and spring selection, different features, such as bi-stable ability or QZS, can be achieved. Then a TS-SMO QZS vibration isolator was designed as an application example of the proposed TS-SMO structure. Both design parameters of the TS-SMO unit structure and the static analysis of the system were presented. The displacement transmissibility under different excitations were investigated under variable viscous system damping. The isolation performance in low frequency range could be ideally improved as any other QZS isolators.

It is hoped that this pioneering TS-SMO base structure developed in this paper could provide a valuable insight for applying the origami structure into real applications, by using simple mechanical components.

Funding

This research did not receive any specific grant from funding agencies in the public, commercial, or not-for-profit sectors.

References

[1] C. Liu, K. Yu, Accurate modeling and analysis of a typical nonlinear vibration isolator with quasi-zero stiffness, Nonlinear Dynamics, (2020) 1-25.
[2] G. Yan, H.-X. Zou, S. Wang, L.-C. Zhao, Q.-H. Gao, T. Tan, W.-M. Zhang, Large stroke quasi-zero stiffness vibration isolator using three-link mechanism, Journal of Sound and Vibration, 478 (2020).
[3] F. Zhao, J. Ji, K. Ye, Q. Luo, Increase of quasi-zero stiffness region using two pairs of oblique springs, Mechanical Systems and Signal Processing, 144 (2020).
[4] F. Zhao, J. Ji, Q. Luo, S. Cao, L. Chen, W. Du, An improved quasi-zero stiffness isolator with two pairs of oblique springs to increase isolation frequency band, Nonlinear Dynamics, 104 (2021) 349-365.
[5] G. Dong, X. Zhang, S. Xie, B. Yan, Y. Luo, Simulated and experimental studies on a high-static-low-dynamic stiffness isolator using magnetic negative stiffness spring, Mechanical Systems and Signal Processing, 86 (2017) 188-203.
[6] Y. Zheng, X. Zhang, Y. Luo, Y. Zhang, S. Xie, Analytical study of a quasi-zero stiffness coupling using a torsion magnetic spring with negative stiffness, Mechanical Systems and Signal Processing, 100 (2018) 135-151.
[7] B. Yan, H. Ma, B. Jian, K. Wang, C. Wu, Nonlinear dynamics analysis of a bi-state nonlinear vibration isolator with symmetric permanent magnets, Nonlinear Dynamics, 97 (2019) 2499-2519.
[8] B. Yan, H. Ma, L. Zhang, W. Zheng, K. Wang, C. Wu, A bistable vibration isolator with nonlinear electromagnetic shunt damping, Mechanical Systems and Signal Processing, 136 (2019).
[9] H. Pu, S. Yuan, Y. Peng, K. Meng, J. Zhao, R. Xie, Y. Huang, Y. Sun, Y. Yang, S. Xie, J. Luo, X. Chen, Multi-layer electromagnetic spring with tunable negative stiffness for semi-active vibration isolation, Mechanical Systems and Signal Processing, 121 (2019) 942-960.
[10] Y. Jiang, C. Song, C. Ding, B. Xu, Design of magnetic-air hybrid quasi-zero stiffness vibration isolation system, Journal of Sound and Vibration, 477 (2020).
[11] W. Zou, C. Cheng, R. Ma, Y. Hu, W. Wang, Performance analysis of a quasi-zero stiffness vibration isolation system with scissor-like structures, Archive of Applied Mechanics, 91 (2020) 117-133.
[12] T. Deng, G. Wen, H. Ding, Z.-Q. Lu, L.-Q. Chen, A bio-inspired isolator based on characteristics of quasi-zero stiffness and bird multi-layer neck, Mechanical Systems and Signal Processing, 145 (2020).
[13] G. Jiang, X. Jing, Y. Guo, A novel bio-inspired multi-joint anti-vibration structure and its nonlinear HSLDS properties, Mechanical Systems and Signal Processing, 138 (2020).
[14] X. Feng, X. Jing, Z. Xu, Y. Guo, Bio-inspired anti-vibration with nonlinear inertia coupling, Mechanical Systems and Signal Processing, 124 (2019) 562-595.
[15] X. Jing, L. Zhang, X. Feng, B. Sun, Q. Li, A novel bio-inspired anti-vibration structure for operating hand-held jackhammers, Mechanical Systems and Signal Processing, 118 (2019) 317-339.
[16] J. C. Ji, Q. Luo, K. Ye, Vibration control based metamaterials and origami structures: A state-of-the-art review, Mechanical Systems and Signal Processing, 161 (2021).
[17] M. Schenk, S. D. Guest, Geometry of Miura-folded metamaterials, Proceedings of the National Academy of Sciences, 110 (2013) 3276-3281.
[18] J. Rommers, G. Radaelli, J. L. Herder, A Design Tool for a Single Vertex Compliant-Facet Origami Mechanism Including Torsional Hinge Lines, Journal of Mechanisms and Robotics, 9 (2017).
[19] S. Sengupta, S. Li, Harnessing the anisotropic multistability of stacked-origami mechanical metamaterials for effective modulus programming, Journal of Intelligent Material Systems and Structures, 29 (2018) 2933-2945.
[20] J. Butler, L. Bowen, E. Wilcox, A. Shrager, M. I. Frecker, P. von Lockette, T. W. Simpson, R. J. Lang, L. L. Howell, S. P. Magleby, A Model for Multi-Input Mechanical Advantage in Origami-Based Mechanisms, Journal of Mechanisms and Robotics, 10 (2018).

[21] H. Banerjee, T. K. Li, G. Ponraj, S. K. Kirthika, C. M. Lim, H. Ren, Origami-Layer-Jamming Deployable Surgical Retractor With Variable Stiffness and Tactile Sensing, Journal of Mechanisms and Robotics, 12 (2020).
[22] L. Howell, S. Magleby, B. Jensen, D. Bailey, K. Seymour, J. Butler, B. Sargent, An Origami-Based Medical Support System to Mitigate Flexible Shaft Buckling, Journal of Mechanisms and Robotics, 12 (2020).
[23] H. Banerjee, N. Pusalkar, H. Ren, Single-Motor Controlled Tendon-Driven Peristaltic Soft Origami Robot, Journal of Mechanisms and Robotics, 10 (2018).
[24] A. Donmez, E. Cigeroglu, G. O. Ozgen, An improved quasi-zero stiffness vibration isolation system utilizing dry friction damping, Nonlinear Dynamics, 101 (2020) 107-121.
[25] H. Yasuda, J. Yang, Reentrant Origami-Based Metamaterials with Negative Poisson's Ratio and Bistability, Physical Review Letters, 114 (2015) 185502.